Structural basis for the conformational changes of insulin receptor induced by three different hormone ligands

Xi Zhang[1,7], Ting Zhang[1,7], Cang Wu[2,7], Yuanzhu,Gao[3,7], Shuo Zhang[6,7], Zhenglin Li[2], Linshan Zhong[1], Chenyu Xia[2], Liuqing,Yang[1], Fengquan Dong[4*], Qing Shu[5*], Yang Fu[1*], Renhong,Yan[1*]

[1]Department of Biochemistry, SUSTech Homeostatic Medicine Institute, School of Medicine, Key University Laboratory of Metabolism and Health of Guangdong, Institute for Biological Electron Microscopy, Southern University of Science and Technology, Shenzhen, 518055, Guangdong, China.

[2]Department of Biology, School of Life Sciences, Southern University of Science and Technology, Shenzhen, 518055, China.

[3]Cryo-EM Centre, Southern University of Science and Technology, Shenzhen, 518055, China;

[4]Cardiovascular medicine, Shenzhen University General Hospital, Shenzhen, 518055, Guangdong, China.

[5]Department of Gastroenterology, The First Affiliated Hospital of Shenzhen University, Shenzhen People's Second Hospital, Shenzhen, 518000, China.

[6]School of Life Sciences, Zhengzhou University, Zhengzhou, Henan Province, China

[7]These authors contribute equally.

[*]To whom correspondence should be addressed: Fengquan Dong Fengquan.dong@foxmail.com (F.D.); sq6060@163.com (Q.S.); fuy@sustech.edu.cn (Y.F.); yanrh@sustech.edu.cn (R.Y.)

Summary

The insulin receptor (IR) is central to the regulation of glucose and lipid metabolism. Although insulin is its primary ligand, insulin-like growth factors I and II (IGF-I and IGF-II) also engage IR, albeit with reduced affinity. The structural basis of cooperative ligand binding, however, has remained poorly understood. Here, we report cryo-Electron Microscopy (cryo-EM) structures of IR in complex with insulin, IGF-I, and IGF-II, revealing that all three ligands engage the receptor at overlapping binding sites and can induce a conserved T-shaped quaternary assembly involving four ligand molecules at site 1/1′ and site 2/2′. Despite this shared overall architecture, distinct ligand-specific conformational changes were observed. Notably, IGF-I and IGF-II adopt different binding sequence at site 1 and site 2 compared to insulin, suggesting unique interaction dynamics. These structural insights highlight divergent mechanisms of ligand recognition and cooperative binding, providing a deeper understanding of hormone-induced conformational modulation of the IR.

Keywords: **Insulin receptor, IGF-I, IGF-II, Cryo-electron microscopy**

Introduction

The insulin receptor (IR) is a transmembrane receptor tyrosine kinase (RTK) that plays a fundamental role in regulating glucose and lipid homeostasis in humans, particularly by mediating insulin-dependent signaling pathways that control glucose uptake, metabolism, and storage in key tissues such as muscle, fat, and liver cells[1-5]. Dysregulation of IR signaling is associated with metabolic disorders including type 2 diabetes mellitus and insulin resistance syndromes, making IR a critical therapeutic target[1, 3, 4].

Research suggests that the IR dimer comprises two identical protomers (protomer A and protomer B), each composed of α- and β-subunits linked by disulfide bonds and exhibiting a Λ-shaped symmetric structure[6-8]. Upon insulin binding to the extracellular domain (ECD) of IR, the signal is transmitted through the transmembrane domain to the intracellular domain, inducing phosphorylation of the tyrosine kinase domain (TK)[7-11]. Insulin binds IR at two primary interaction sites, the site 1 and site 2, each present on both protomers, resulting in a total of four potential ligand-binding sites per receptor dimer (site 1/1′ and site 2/2′). Cryo-EM studies have revealed both asymmetric (*T*-shaped) and symmetric (T-shaped) conformations of IR in complex with insulin, corresponding to partially and fully active signaling states, respectively[10,11].

In addition to insulin, IR can also bind insulin-like growth factors I and II (IGF-I and IGF-II), although these interactions occur with lower affinity[12]. Recent reviews have comprehensively summarized advances in the structural and biochemical understanding of insulin and IGF receptor activation mechanisms[13, 14], highlighting the conserved architecture of the

insulin/IGF signaling axis. However, the molecular basis of ligand recognition and cooperative binding, particularly for IGF-I and IGF-II interaction with IR, remains incompletely understood. IGF-I and IGF-II share high sequence and structural similarity with insulin and act primarily through their cognate receptors, IGF-IR and IGF-IIR, respectively[15-19] (Fig.S1). However, their capacity to engage IR, particularly the IR-A isoform, which lacks exon 11 and is frequently expressed in fetal tissues and cancer, suggests potential physiological and pathological roles in modulating IR activity, remains unclear[20-23]. Despite extensive structural studies have elucidated IR–insulin complexes and, more recently, IGF-II bound IR structures, establishing a general framework for receptor activation[24,25], how IGF-I and IGF-II bind to full-length IR-A and induce cooperative or distinct conformational changes remains largely unexplored.

To address this gap, we determined cryo-EM structures of full-length human IR-A bound to insulin, IGF-I, and IGF-II. While insulin- and IGF-II-bound IR structures have been characterized previously[25], the molecular basis of IGF-I recognition by full-length IR-A has remained elusive. Previous structural information was limited to an IR-B/IGF-1R hybrid receptor, in which a single IGF-I molecule occupied site 1[26]. Here, we present the first cryo-EM structures of full-length IR-A in complex with IGF-I, revealing that IR-A can accommodate up to three IGF-I molecules at sites 1 and 2. Taken together, these data uncover ligand-dependent local conformational differences and provide a structural framework for understanding ligand-specific IR activation and cooperativity.

METHOD DETAILS

Protein expression and purification

Full-length human IR-A (accession number: NM_001079817.3) with 3 X Flag-Affinity Tag at the C-terminal tail was subcloned into the pCDNA3.1 expression vector. The receptor was expressed by HEK293F cells that were grown at 37 ℃ in SMM-293T-II expression medium (Sino Biological). When the cell density reached to 2-3 × 10^6 cells/ml, the cells were transiently transfected with 1 mg/l endotoxin-free plasmid (mixed with polyethyleneimine, 1:3 [w/w] ratio), maintained for 72 h at 30 ℃, and harvested by centrifugation (1500 × g, 3 min). The cells were resuspended in lysis buffer containing 25 mM Tris-HCl pH 8.0, 200 mM NaCl, 1.0% (w/v) DDM (ndodecyl-b-D-maltopyranoside, APExBIO), and protease inhibitor cocktail (APExBIO) and harvested by centrifugation (100,000 × g, 1 h). The supernatant was collected and incubated with anti-DYKDDDDK affinity beads (Smart-Lifesciences) and then washed with more than 10 column volumes of washing buffer [PBS buffer with 0.1% (w/v) DDM (n-dodecyl-b-D-maltopyranoside, APExBIO) and 1X protease inhibitor cocktail]. Finally, the targeted protein was eluted by 0.2 mg/ml Flag peptides and further purified by size exclusion chromatography (Superose 6 10/300 GL, Cytiva Healthcare) in PBS buffer with 0.03% (w/v) DDM. For cryo-EM sample preparation, the IR protein was mixed with Amphipol A8-35 at 1:5 (w/w) with gentle rotation for approximately 12 h, and then Bio-Beads SM-2 (BIO-RAD) was added to remove superfluous detergent. Finally, the Bio-Beads were removed by centrifugation, and the protein was further purified by a Superose 6 increase 10/300 GL size-exclusion column. Insulin (Sigma-Aldrich, Cat#91077C), IGF-I (Sino Biological Cat#CU100) and IGF-II (Sino Biological, Cat#

FU100) dry powder were dissolved and further purified by size-exclusion chromatography with PBS buffer.

EM data acquisition, model building and refinement

A 3 μL concentrated samples (IR:insulin/IGF-I/IGF-II, with a molar ratio of 1:1-6) were added to the glow-discharged Quantifoil R1.2/1.3 300-mesh gold holey carbon grids (Quantifoil). Grids were waited for 3.0 s and blotted for 3.0 s under 100% humidity at 4 ℃ before being plunged into liquid ethane by a Vitrobot (FEI). Micrographs were acquired on a Titan Krios microscope (FEI) operated at 300 kV with a K3 Summit direct electron detector (Gatan), yielding a pixel size of 0.66 Å on images. The defocus range was set from -1.0 to -2.5 mm. Each micrograph was dose-fractionated to 32 frames under a dose rate of 20 e^-/pixel/s, with a total exposure time of 1.08 s. All steps of image processing were performed using cryoSPARC software tools[27,28] (Fig. S3-S9). All resolutions were estimated by applying a soft mask around the protein density using the gold-standard Fourier shell correlation (FSC, 0.143)[29]. Models from the (AlphaFold2AF-P06213-F1-model_v4.pdb) and previously reported structures (PDB: 5U8Q, 6PXW, 6VWG and 6PXV) were initiated by docking each domain derived into the cryo-EM map by UCSF ChimeraX software, further adjusted in Coot[30-32]. Finally, the model was refined by Phenix software[33].

Data availability

Atomic coordinates and cryo-EM density maps of the IR/IGF-I complexes (PDB: 8XJS, whole map: EMD-38404; PDB: 8XK1, whole map: EMD-38413; PDB: 8XKR, whole map: EMD-38423; PDB: 8XKM, whole map: EMD-38420), the IR/insulin complexes (PDB: 8YYL, whole map: EMD-39675; PDB: 8YYS, whole map: EMD-39677; PDB:

8YYT, whole map: EMD-39678), and the IR/IGF-II complexes (PDB: 8YSZ, whole map: EMD-39566) have been deposited to the Protein Data Bank (http://www.rcsb.org) and the Electron Microscopy Data Bank (https://www.ebi.ac.uk/pdbe/emdb/), respectively (Table S1). And all maps and coordinates are available from the corresponding authors upon reasonable request.

RESULTS

Cryo-EM structures of the IR bound to different hormones

To elucidate the structural basis of IGF-I binding to the IR, we performed single-particle cryo-EM analysis of full-length IR in the presence of saturating concentrations of IGF-I, using molar ratios of 1:6 and 1:12 (IR:IGF-I). These datasets revealed multiple conformational states, with three or four IGF-I molecules bound. By combining particles from both conditions, we obtained four distinct reconstructions at resolutions of 3.24 Å, 3.53 Å, 5.00 Å, and 3.31 Å, enabling detailed structural analysis (Fig.1, Fig. S2-S4).

To capture lower-occupancy states, we also analyzed IR in the presence of reduced IGF-I concentrations (1:3 molar ratio). Across all tested conditions, two predominant conformations consistently emerged: an asymmetric state with two IGF-I molecules bound, and a symmetric T-shaped state with four IGF-I molecules bound (Fig. S4). In the asymmetric conformation, IGF-I molecules occupy binding site 1 and site 2 on protomer A, while site 1′ and site 2′ on protomer B remain unoccupied, resulting in increased flexibility in the CR–L1 domains of protomer A and the FnIII-1 to -3 domains of protomer B (Fig.1). In contrast, the symmetric T-shaped conformation displays all four IGF-I molecules bound at site 1/1′ and site 2/2′, stabilizing the extracellular domains (Fig.S8).

We next investigated the interaction between IR and IGF-II, a structurally homologous ligand of IGF-I. Cryo-EM analysis of IR in complex with IGF-II at a 1:6 molar ratio revealed two main conformations: an asymmetric state with two IGF-II molecules (3.35 Å, predominant class) and a symmetric T-shaped conformation with four IGF-II molecules (approximately 8 Å). Although the latter exhibited lower resolution, IGF-II densities near the FnIII-1 domains were clearly discernible (Fig. S7). These conformations were largely consistent with those observed in the IR/IGF-I complex (Fig. S3–S4). Interestingly, in the asymmetric IR/IGF-II structure, the FnIII-3/FnIII-3′ domains showed tight inter-protomer contacts, differing from a recently reported structure (Fig. S10). Attempts to capture lower-occupancy states at reduced IGF-II concentrations were unsuccessful, suggesting that IGF-II preferentially stabilizes asymmetric T-shaped states over the symmetric T-shaped conformation.

To directly compare ligand-induced binding patterns, we also determined the cryo-EM structures of IR in complex with insulin at molar ratios of 1:3 and 1:6 under identical experimental conditions (Fig.1 and Fig. S5-S6). As expected, increasing insulin concentrations correlated with greater ligand occupancy, resulting in three predominant conformational states: IR bound to one, two, or four insulin molecules (Fig. S9). At low insulin concentrations (1:3), a T-shaped conformation with insulin bound only to site 1 and site 1′ was readily detected (Fig. S6). In contrast, under saturating conditions, only the fully active T-shaped conformation with four insulin molecules bound was observed, consistent with previous reports (Fig. S5)[10]. Notably, in the singly bound IR-insulin structure, significant flexibility was observed in the FnIII-2′ and

FnIII-3′ domains of protomer B. In contrast, the T-shaped conformations with two or four insulin molecules exhibited comparable overall architectures, representing fully active states of the receptors (Fig.S9)[11].

A comparative analysis of ligand binding sequences revealed distinct ligand-specific dynamics. For IGF-I, occupation of site 1 is followed by binding at site 2, with subsequent engagement of site 1′ and site 2′ at higher ligand concentrations. This binding order contrasts with that of insulin, which has been proposed to initially engage site 2′ in the membrane-proximal FnIII-1′ domain before transitioning to site 1 formed by the L1 domain, α-CT′, and FnIII-1′, as proposed by Nielsen[34]. Similarly, IR bound to IGF-II at a 1:6 molar ratio exhibited two structural states, one with IGF-II molecules occupying site 1 and site 2, and another with all four sites occupied, suggesting a binding sequence analogous to that of IGF-I (Fig. S7, S10). These ligand-specific binding behaviors likely contribute to their divergent physiological roles and downstream signaling outputs[4, 19].

Interaction interfaces for different hormones at binding site 1

To elucidate the molecular determinants underlying hormone recognition by the IR, we focused on the detailed interaction interfaces at binding site 1, a critical region that initiates ligand-induced conformational changes. In contrast, binding site 1′ and site 2/2′ exhibited relatively weak ligand densities (Fig. S8-S10), highlighting the central role of site 1 in hormone engagement.

At binding site 1, a composite binding pocket is formed by three structural elements: the L1 domain from protomer A, the α-CT′ helix, and the FnIII-1′ domain from protomer B. Together, these elements delineate a binding cavity composed of at least 20 interface residues

that accommodate hormone molecules[11]. In the IR/insulin complex, key residues contributing to the binding pocket include Asn42, Glu61, and Lys148 from the L1 domain; Arg744, Glu733, and Glu738 from the α-CT′ helix; and Asn568 from the FnIII-1′ domain. For the IR/IGF-I complex, the pocket is formed by Asn42, Arg41, and Glu343 from the L1 domain; Asn738 and Arg744 from the α-CT′ helix; and Arg566 from the FnIII-1′ domain. Similarly, in the IR/IGF-II complex, the binding pocket comprises Asn42, Lys67, and Gly37 from the L1 domain; Arg744 and Glu738 from the α-CT′ helix; and Pro522 from the FnIII-1′ domain (Fig. 2A-C).

Notably, Arg744 and Glu738 of the α-CT′ helix, together with Asn42 from the L1 domain, are consistently involved in binding all three hormones, indicating a conserved recognition mechanism at site 1. Among the tested ligands, insulin demonstrated the highest binding affinity, as reflected by the greater number of hydrogen bonds formed, which is consistent with previous observations[15].

The conformational changes of the IR/IGF-I and IR/Insulin complexes

We next examined the overall conformational changes of the IR upon IGF-I binding. Notably, the transient occupancy of binding site 1/2, an interface between sites 1 and 2, by a third and fourth IGF-I molecule introduces substantial flexibility to surrounding domains prior to the establishment of the canonical T-shaped conformation (Fig. 3). This increased flexibility is particularly evident in the FnIII-1, FnIII-2, and FnIII-3 domains of protomer A, as well as the L1 domain of protomer B, all of which undergo marked shifts despite the inherent symmetry of the IR dimer (Fig. 3).

In contrast, the IR–insulin complex exhibits greater conformational

stability across different ligand-bound states. Specifically, the L1, CR, and L2 domains of protomer A, together with the α-CT' helix and FnIII-1' domain of protomer B, remain largely unaltered upon binding one, two, or four insulin molecules, owing to insulin's high-affinity engagement at binding site 1 (Fig. 4).

We further compared the fully ligand-bound T-shaped conformations of the IR/IGF-I and IR/insulin complexes. Overall, the symmetric structures are highly similar, particularly in the head region encompassing the L1, CR, L2, FnIII-1 domains and α-CT helix. However, when aligned by protomer A, clear differences emerge in the relative positioning of the two FnIII domains, especially in their interdomain distances (Fig. S11).

Interestingly, we did not observe any structures of IR bound with two IGF-I or IGF-II molecules both occupying binding site 1 and site 1′. Instead, an asymmetric conformation was consistently observed, wherein the two hormone molecules occupy binding sites 1 and 2 of protomer A, even at a 1:3 ligand-to-receptor ratio. These findings suggest hormone-specific conformational dynamics during IR activation, pointing to distinct mechanisms of receptor engagement and activation by insulin, IGF-I, and IGF-II, which may underlie their differential physiological functions.

Discussion

Insulin-like growth factors are secreted at relatively stable levels, in contrast to the rapid and transient fluctuations of insulin. Consistent with this physiological difference, our structures show that the predominant conformations of the IR/IGF-I complex remain largely unchanged across varying ligand concentrations. This concentration-independent behavior suggests that IGF-I promotes a

more sustained and stable mode of receptor activation, potentially supporting long-term cellular functions such as growth, differentiation, and metabolism, rather than acute regulation of glucose homeostasis.

It should be emphasized that the cryo-EM structures presented here were obtained under *in vitro* conditions using elevated ligand concentrations to stabilize distinct receptor-bound states. These structures therefore define the conformational space accessible to the insulin receptor upon ligand engagement, rather than representing the dominant signaling states under physiological conditions.

By comparison, the canonical T-shaped conformation of the IR/insulin complex is only stabilized under saturating insulin conditions, reflecting a concentration-dependent mechanism that aligns with the rapid and tightly regulated demands of glucose homeostasis. Although the overall assemblies of IR bound to insulin, IGF-I, IGF-II, and insulin-like polypeptides appear similar, their dynamic conformational transitions differ in a ligand-specific manner[25,35,36].

An intriguing finding is that IGF-I can occupy all four receptor binding sites more readily than insulin, despite insulin having a higher overall binding affinity for IR. This apparent paradox may be explained by differential site specific affinities, particularly at binding site 1′ and 2. Previous biochemical studies have established that insulin receptor activation involves two spatially distinct but functionally coupled binding surfaces and exhibits pronounced negative cooperativity, such that differences in site-specific engagement can substantially influence ligand occupancy and conformational outcomes [37]. Moreover, recent structural and

functional analyses have suggested that insulin and IGF ligands differ in their reliance on site-2 engagement, providing a mechanistic basis for ligand-specific cooperativity and activation pathways[25]. Our structural data suggest that IGF-I binds to site 2 and site 1′ more efficiently than insulin, facilitating the formation of fully occupied symmetric conformations even at lower ligand concentrations. Based on these findings, we propose a dynamic combinatorial binding model to account for the ligand-specific occupancy patterns and conformational transitions of IR upon binding insulin, IGF-I, or IGF-II (Fig.5). This model highlights the importance of individual binding site affinities and local flexibility in shaping the overall activation mechanism of the receptor.

Comparison with previously reported insulin receptor complexes further contextualizes our findings. The insulin-bound structures[10,11] and the IGF-II:IR-B complexes[25] collectively revealed conserved features of ligand-induced activation, while the hybrid IR-B/IGF-1R:IGF-I structures[26] demonstrated that IGF-I engages only a single site on the hybrid receptor. Our full-length IR-A:IGF-I structures extend these observations by showing multi-ligand occupancy and a distinct mode of cooperative activation not previously observed for IGF ligands.

These results, together with the binding sequence model proposed by Nielsen[34] and the comprehensive structural perspectives summarized in[13,14], provide an integrated view of ligand recognition within the insulin receptor family. Collectively, this study advances our understanding of how insulin, IGF-I, and IGF-II differentially modulate IR activation and signaling specificity.

ACKNOWLEDGMENTS

We thank Shuman Xu, Lei Zhang, Yuanzhu Gao, and Peiyao Li at the Cryo-EM Center of SUSTech for technical support in electron microscopy data acquisition. Renhong Yan is an investigator of SUSTech Institute for Biological Electron Microscopy. This project was mainly supported by the National Natural Science Foundation of China (32422039 to R.Y.), the Shenzhen Science and Technology Program (RCYX20231211090342048 to R.Y.), the Shenzhen Medical Research Fund (A2303046 and B2402043 to R.Y.), the Major Talent Recruitment Program of Guangdong Province (2021QNO2Y167 to R.Y.), the Medical Scientific Research Foundation of Guangdong Province of China (No.A2021333 to F.Q.D.), Shenzhen Science and Technology Innovation Commission Project (No.JCYJ20190808120613189 to F.Q.D.), Shenzhen science and technology research and development fund project (NO.KCXFZ20201221173208023-1039027 to Q.S.), the Shenzhen Pea-cock Team Project (KQTD20200909113758004 to Y.F.). And Special thanks to the support of Taidu Biotech(Suzhou)Co.,Ltd. in protein purification equipments.

AUTHOR CONTRIBUTIONS

R.Y. and X.Z. conceived the project. R.Y., Y.F, Q.S., and D.F. supervised the project. R.Y., Y.F, Q.S., D.F., S.Z., and X.Z. designed the experiments. T.Z. did the model analysis. All authors did the experiments and contributed to data analysis. R.Y. and X.Z. wrote the manuscript. R.Y., X.Z., and S.Z. revised the manuscript.

DECLARATION OF INTERESTS

The authors declare no competing interests.

References

1. Kasuga, Karlsson, Kahn. Insulin stimulates the phosphorylation of the 95,000-dalton subunit of its own receptor. Science. 1982,215:185-187.
2. Ebina, Ellis, Jarnagin, Edery, Graf, Clauser, Ou, et al. The human insulin receptor cDNA: the structural basis for hormone-activated transmembrane signalling. Cell. 1985,40:747-758.
3. Zhang, Zhu, Bi, Huang, Zhou. The Insulin Receptor: An Important Target for the Development of Novel Medicines and Pesticides. Int J Mol Sci. 2022,23.
4. Lawrence. Understanding insulin and its receptor from their three-dimensional structures. Mol Metab. 2021,52:101255.
5. Wei, Lu, Yao, Hong, Yang, Zhang, Yin, et al. Insight into Janus Kinases Specificity: From Molecular Architecture to Cancer Therapeutics. MedComm – Oncology. 2024,3.
6. McKern, Lawrence, Streltsov, Lou, Adams, Lovrecz, Elleman, et al. Structure of the insulin receptor ectodomain reveals a folded-over conformation. Nature. 2006,443:218-221.
7. Xiong, Blakely, Kim, Menting, Schafer, Schubert, Agrawal, et al. Symmetric and asymmetric receptor conformation continuum induced by a new insulin. Nat Chem Biol. 2022,18:511-519.
8. Li, Park, Mayer, Webb, Uchikawa, Wu, Liu, et al. Synergistic activation of the insulin receptor via two distinct sites. Nat Struct Mol Biol. 2022,29:357-368.
9. Choi, Bai. The Activation Mechanism of the Insulin Receptor: A Structural Perspective. Annu Rev Biochem. 2023,92:247-272.
10. Uchikawa, Choi, Shang, Yu, Bai. Activation mechanism of the insulin receptor revealed by cryo-EM structure of the fully liganded receptor-ligand complex. Elife. 2019,8.

11. Scapin, Dandey, Zhang, Prosise, Hruza, Kelly, Mayhood, et al. Structure of the insulin receptor-insulin complex by single-particle cryo-EM analysis. Nature. 2018,556:122-125.
12. Firth, Baxter. Cellular actions of the insulin-like growth factor binding proteins. Endocr Rev. 2002,23:824-854.
13. Van-Duyne, Blair, Sprenger, Moiseenkova-Bell, Plymate, Penning. The androgen receptor. Vitam Horm. 2023,123:439-481.
14. Forbes. The three-dimensional structure of insulin and its receptor. Vitam Horm. 2023,123:151-185.
15. Morrione, Valentinis, Xu, Yumet, Louvi, Efstratiadis, Baserga. Insulin-like growth factor II stimulates cell proliferation through the insulin receptor. P Natl Acad Sci USA. 1997,94:3777-3782.
16. Hawkes, Kar. The insulin-like growth factor-II/mannose-6-phosphate receptor: structure, distribution and function in the central nervous system. Brain Res Rev. 2004,44:117-140.
17. Kasprzak. Insulin-Like Growth Factor 1 (IGF-1) Signaling in Glucose Metabolism in Colorectal Cancer. Int J Mol Sci. 2021,22.
18. Zhu, Chen, Song, Cui, Chen, Yu, Song. Insulin-like Growth Factor-2 (IGF-2) in Fibrosis. Biomolecules. 2022,12.
19. LeRoith, Holly, Forbes. Insulin-like growth factors: Ligands, binding proteins, and receptors. Mol Metab. 2021,52:101245.
20. Escribano, Beneit, Rubio-Longas, Lopez-Pastor, Gomez-Hernandez. The Role of Insulin Receptor Isoforms in Diabetes and Its Metabolic and Vascular Complications. J Diabetes Res. 2017,2017:1403206.
21. Vella, Giuliano, La Ferlita, Pellegrino, Gaudenzi, Alaimo, Massimino, et al. Novel Mechanisms of Tumor Promotion by the Insulin Receptor Isoform A in Triple-Negative Breast Cancer Cells. Cells. 2021,10.

22. Denley, Wallace, Cosgrove, Forbes. The insulin receptor isoform exon 11- (IR-A) in cancer and other diseases: a review. Horm Metab Res. 2003,35:778-785.
23. Belfiore, Malaguarnera, Vella, Lawrence, Sciacca, Frasca, Morrione, et al. Insulin Receptor Isoforms in Physiology and Disease: An Updated View. Endocr Rev. 2017,38:379-431.
24. Choi, Duan, Bai. Regulation and function of insulin and insulin-like growth factor receptor signalling. Nat Rev Mol Cell Biol. 2025,26:558-580.
25. An, Hall, Li, Hung, Wu, Park, Wang, et al. Activation of the insulin receptor by insulin-like growth factor 2. Nat Commun. 2024,15:2609.
26. Xu, Margetts, Venugopal, Menting, Kirk, Croll, Delaine, et al. How insulin-like growth factor I binds to a hybrid insulin receptor type 1 insulin-like growth factor receptor. Structure. 2022,30:1098-1108 e1096.
27. Punjani, Rubinstein, Fleet, Brubaker. cryoSPARC: algorithms for rapid unsupervised cryo-EM structure determination. Nat Methods. 2017,14:290-296.
28. Punjani, Zhang, Fleet. Non-uniform refinement: adaptive regularization improves single-particle cryo-EM reconstruction. Nat Methods. 2020,17:1214-1221.
29. Rosenthal, Henderson. Optimal determination of particle orientation, absolute hand, and contrast loss in single-particle electron cryomicroscopy. J Mol Biol. 2003,333:721-745.
30. Goddard, Brilliant, Skillman, Vergenz, Tyrwhitt-Drake, Meng, Ferrin. Molecular Visualization on the Holodeck. J Mol Biol. 2018,430:3982-3996.

31. Jumper, Evans, Pritzel, Green, Figurnov, Ronneberger, Tunyasuvunakool, et al. Highly accurate protein structure prediction with AlphaFold. Nature. 2021,596:583-589.
32. Emsley, Lohkamp, Scott, Cowtan. Features and development of Coot. Acta Crystallogr D Biol Crystallogr. 2010,66:486-501.
33. Liebschner, Afonine, Baker, Bunkoczi, Chen, Croll, Hintze, et al. Macromolecular structure determination using X-rays, neutrons and electrons: recent developments in Phenix. Acta Crystallogr D Struct Biol. 2019,75:861-877.
34. Nielsen, Brandt, Boesen, Hummelshoj, Slaaby, Schluckebier, Nissen. Structural Investigations of Full-Length Insulin Receptor Dynamics and Signalling. J Mol Biol. 2022,434:167458.
35. Viola, Frittmann, Jenkins, Shafi, De Meyts, Brzozowski. Structural conservation of insulin/IGF signalling axis at the insulin receptors level in and humans. Nature Communications. 2023,14.
36. Chen, Chen, Zhao, Li, Ying, Yu, Yan, et al. Real-time artificial intelligence assisted insulin dosage titration system for glucose control in type 2 diabetic patients: a proof of concept study. Oral Science and Homeostatic Medicine. 2023,2.
37. De Meyts. Insulin/receptor binding: the last piece of the puzzle? What recent progress on the structure of the insulin/receptor complex tells us (or not) about negative cooperativity and activation. Bioessays. 2015,37:389-397.

Figure Legends

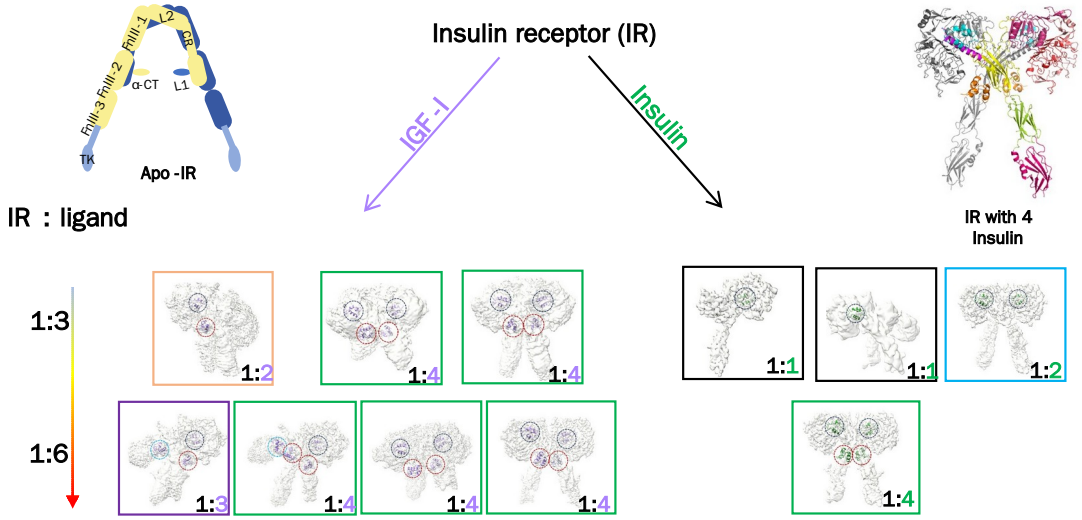

Fig. 1 Cryo-EM structures of the IR bound to insulin or IGF-I across a ligand concentration series.

Representative reconstructions illustrate different ligand-occupancy states of the IR dimer obtained under increasing concentrations of insulin or IGF-I. The occupancy label (e.g., 1:2, 1:3, 1:4) denotes the number of bound ligands per IR dimer in the corresponding structure.

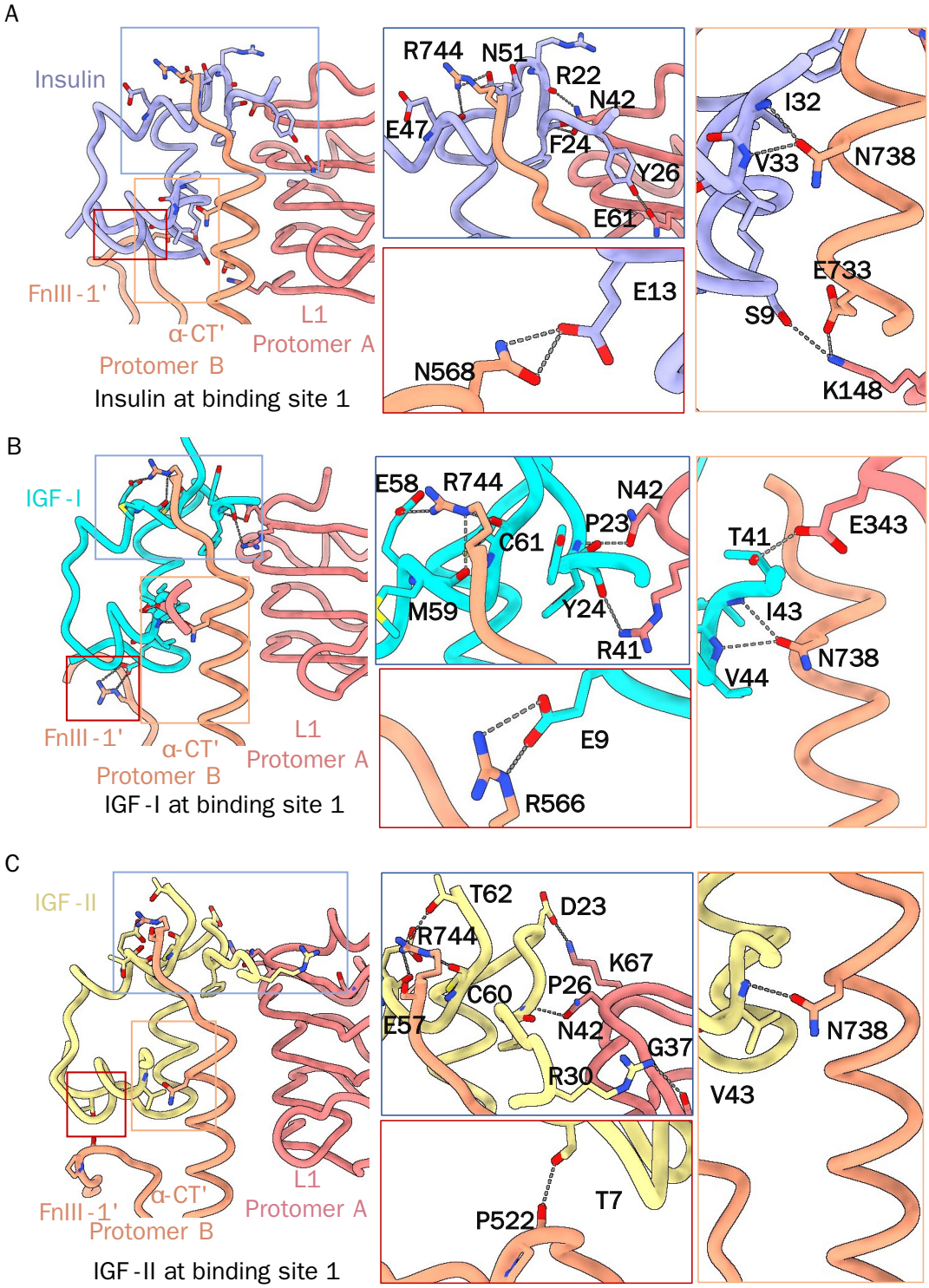

Fig. 2 Interaction interfaces for different hormones at binding site 1.

The insulin, IGF-I and IGF-II were colored as light purple, cyan and yellow, while the protomer A and protomer B were marked as light

orange and light red, respectively.

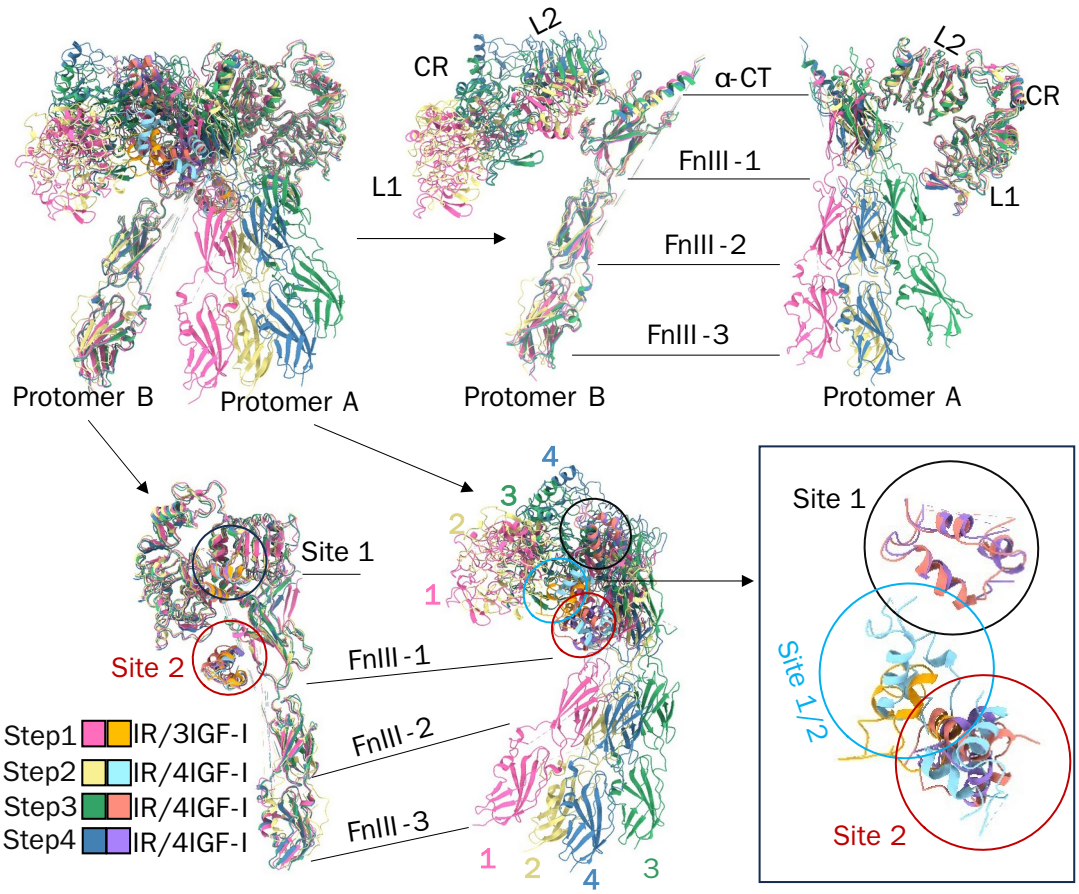

Fig. 3 Structural comparison of IR–IGF-I complexes in different conformational states.

Protomer A and protomer B of the IR dimer are indicated in all panels. The IR protomers are shown in pink, yellow, green, and dark blue, respectively, while the corresponding bound IGF-I molecules are colored orange, cyan, salmon, and purple. Structural superposition of IR–IGF-I complexes reveal a series of distinct conformational states of the receptor associated with increasing ligand occupancy.

Based on these structures, a putative conformational progression is proposed. **Step 1**, one IGF-I molecule is observed at the site 1/2 region. Steps 2–3, two IGF-I molecules bind at distinct positions corresponding to site 1 and site 2, accompanied by local

545 rearrangements of the αCT helix and the FnIII-1 domain of protomer
546 B. Step 4, the extracellular “head” region (L1, CR, L2, FnIII-1, αCT
547 helix, and IGF-I) becomes stabilized, while the relative flexibility of
548 the FnIII-2 and FnIII-3 domains of protomer B is reduced.

549

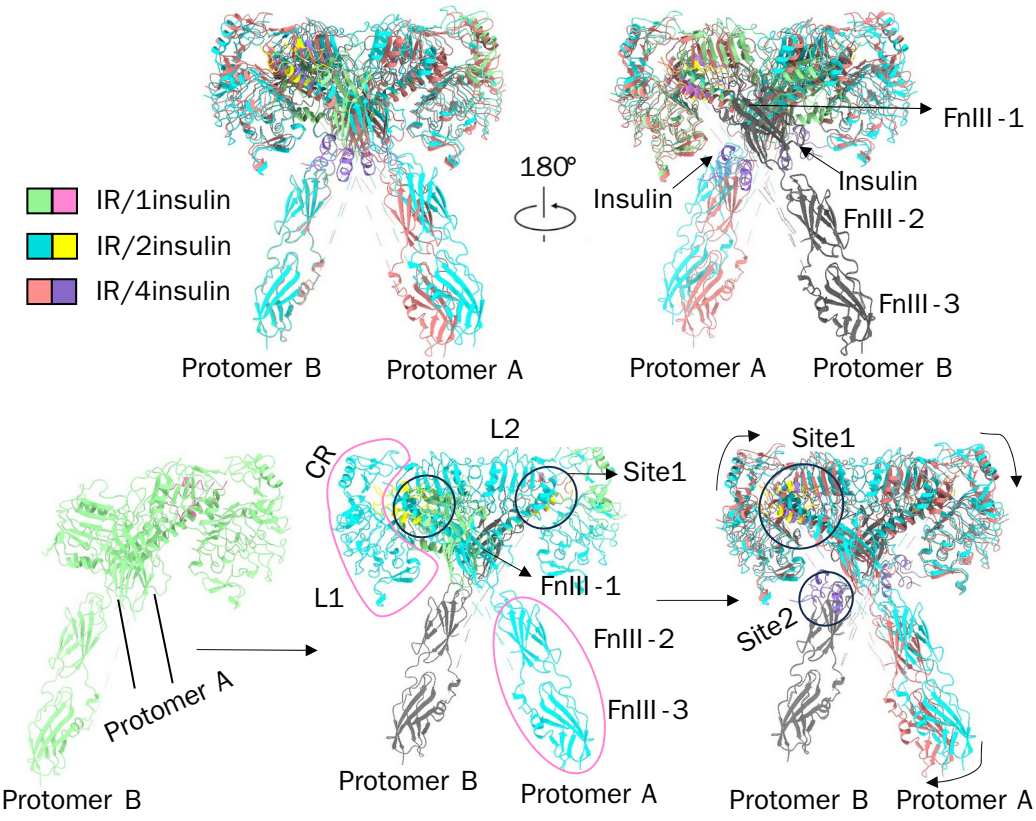

550

551 **Fig. 4 Conformational changes of IR in complex with insulin.**
552 The IR dimers are shown in light green, cyan, and salmon, with the
553 corresponding bound insulin molecules colored pink, yellow, and
554 purple, respectively. Regions showing minimal conformational
555 changes among these insulin-bound states, including FnIII-1,
556 FnIII-2, and FnIII-3, are shown in gray.
557 During the transition from the one-insulin to the two-insulin
558 occupancy state, regions undergoing notable conformational
559 rearrangements are highlighted by pink boxes. In the four-insulin

bound state, both protomer A and protomer B undergo coordinated movements, resulting in a more stabilized overall receptor conformation.

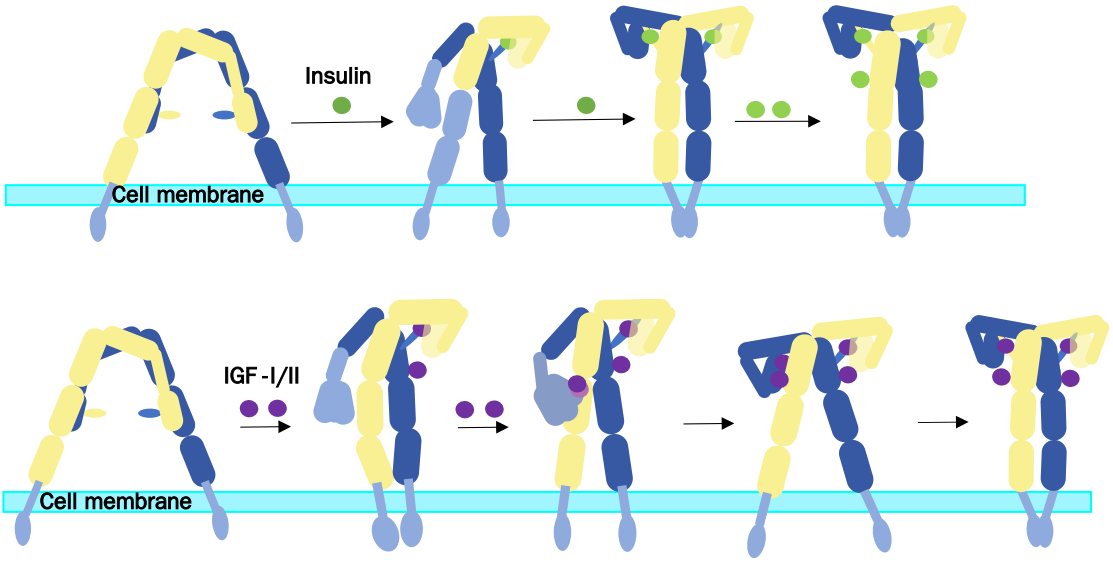

Fig. 5 The working models of how different hormone ligands binds to IR.

Schematic models summarize the proposed activation of IR upon binding insulin or insulin-like growth factors (IGF-I/IGF-II). Insulin and IGFs are shown as green and purple spheres, respectively. The light-blue region indicates flexible parts with lower local resolution in the cryo-EM reconstructions.

Supplementary information

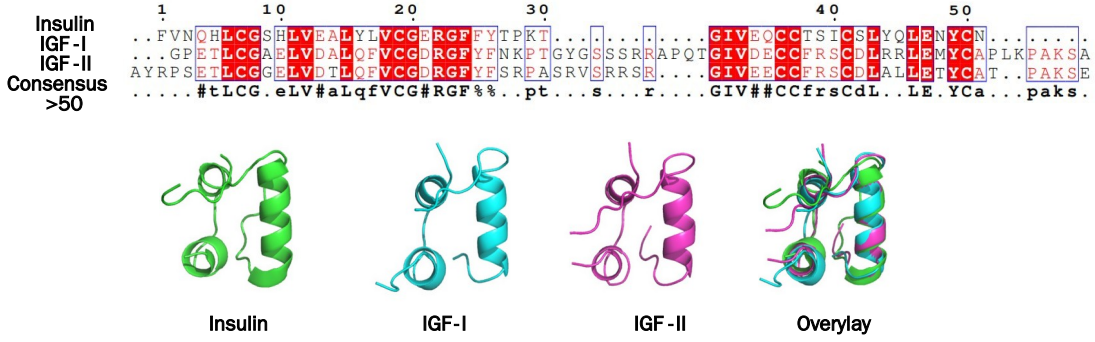

Fig. S1 Sequence alignment and structural comparison for insulin, IGF-I, and IGF-II.

Residues that are identical or conserved in two sequences are colored in red, and the common conserved sequences are labeled with blue boxes. Meanwhile, the structures of insulin, IGF-I, and IGF-II were colored as green, cyan and pink, respectively.

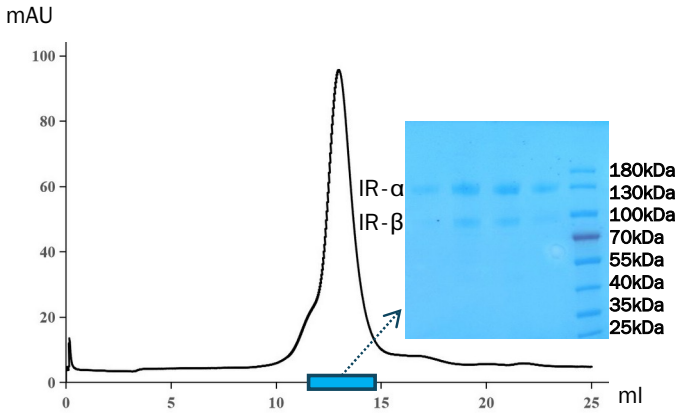

Fig. S2 Protein purification of the full-length human IR.

After the Size-exclusion chromatography, the purity of human IR protein was examined by SDS- PAGE analysis.

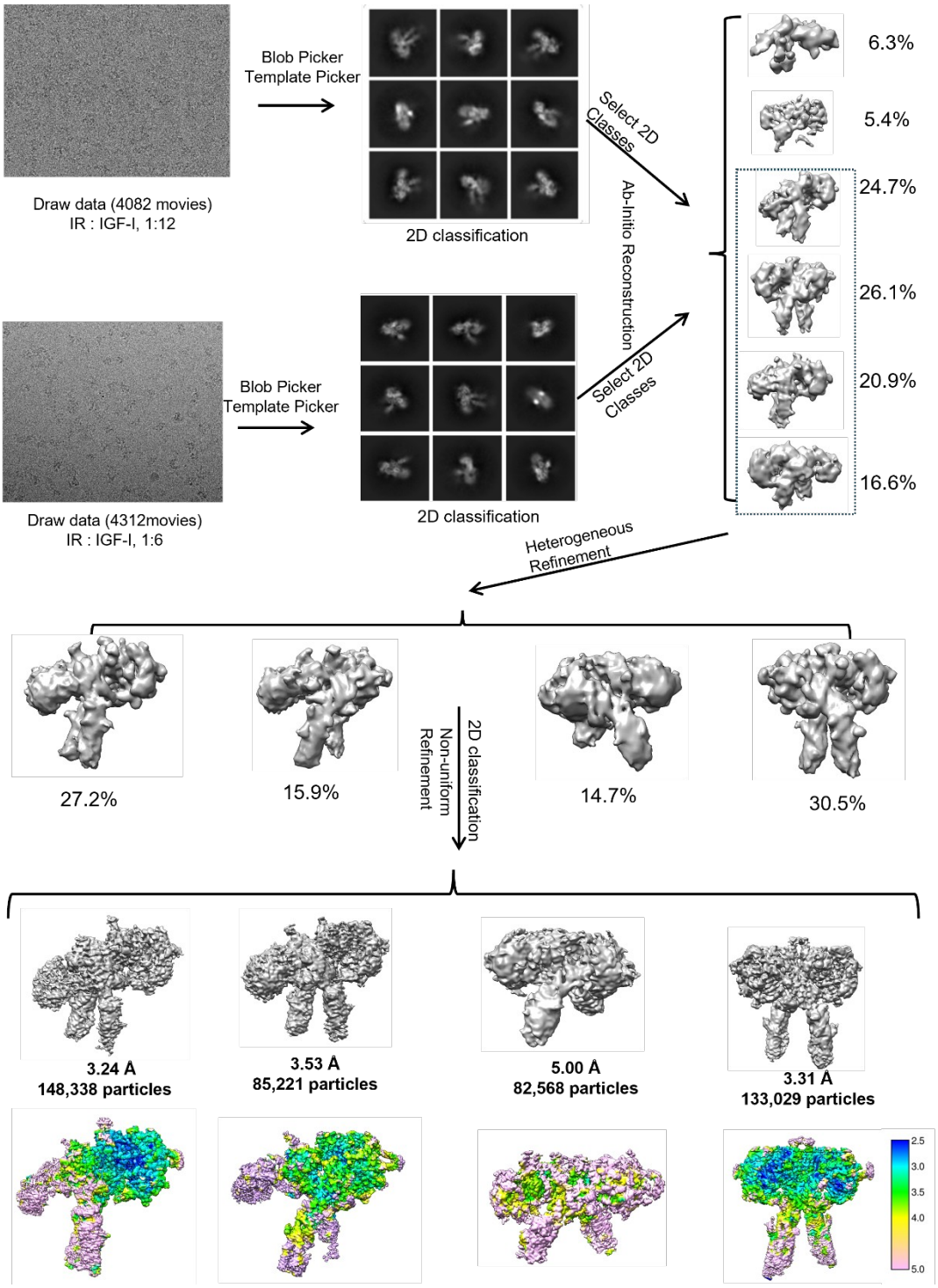

Fig. S3 Cryo-EM data processing flowchart of the IR/IGF-I mixture at a molar ratio of 1:6 (12).

The final three-dimensional reconstructed maps colored according to local resolution were showed directly below the original maps, respectively.

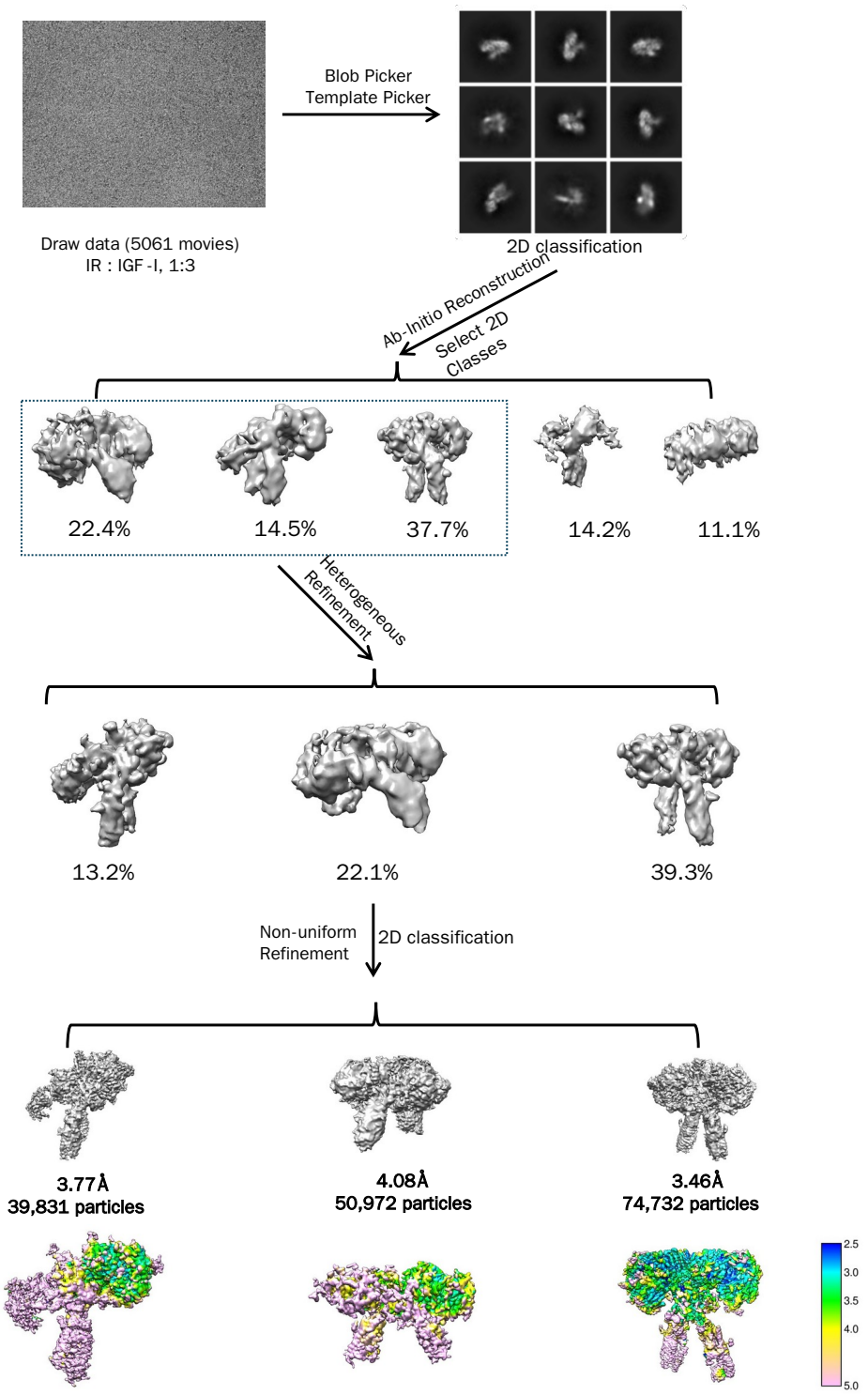

Fig. S4 Cryo-EM data processing flowchart of the IR/IGF-I mixture at a 1:3 molar ratio.

The final three-dimensional reconstructed maps colored according to

local resolution were showed directly below the original maps, respectively.

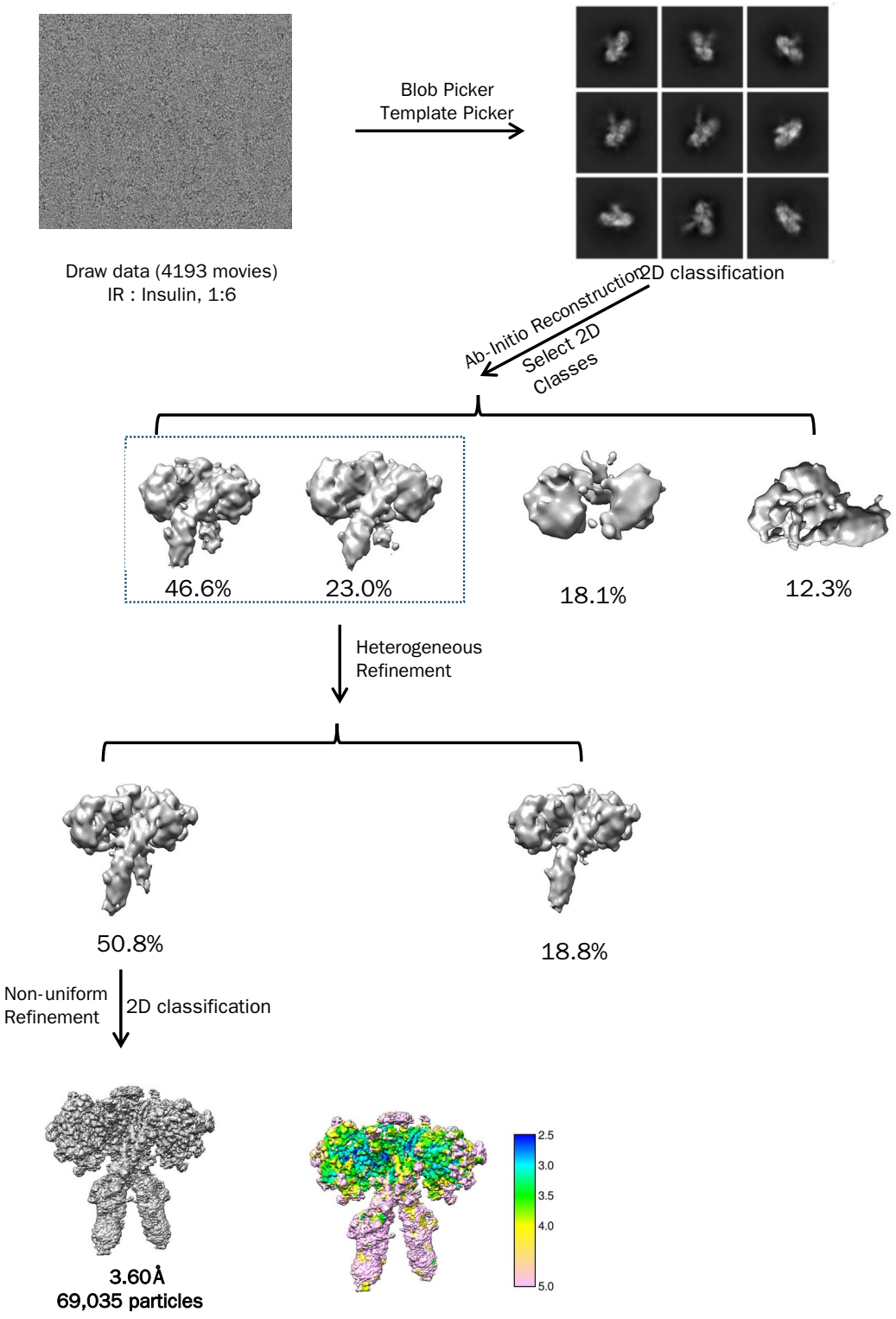

Fig. S5 Cryo-EM data processing flowchart of the IR/insulin mixture at a molar ratio of 1:6.

The final three-dimensional reconstructed map colored according to local resolution was showed next to the original map.

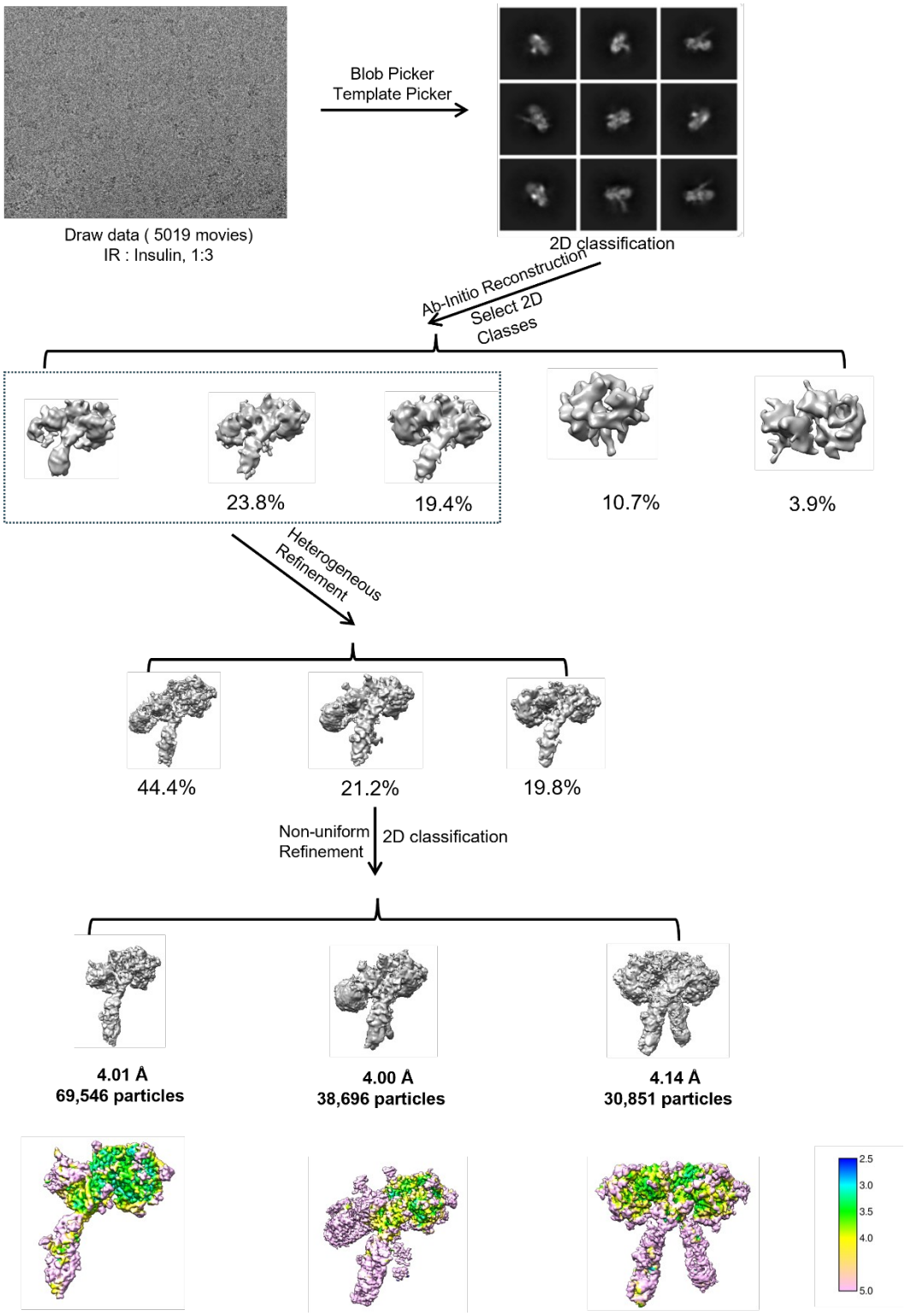

Fig. S6 Cryo-EM data processing flowchart of the IR/insulin mixture at a molar ratio of 1:3.

606 The final three-dimensional reconstructed maps colored according to
607 local resolution were showed directly below the original maps,
608 respectively.

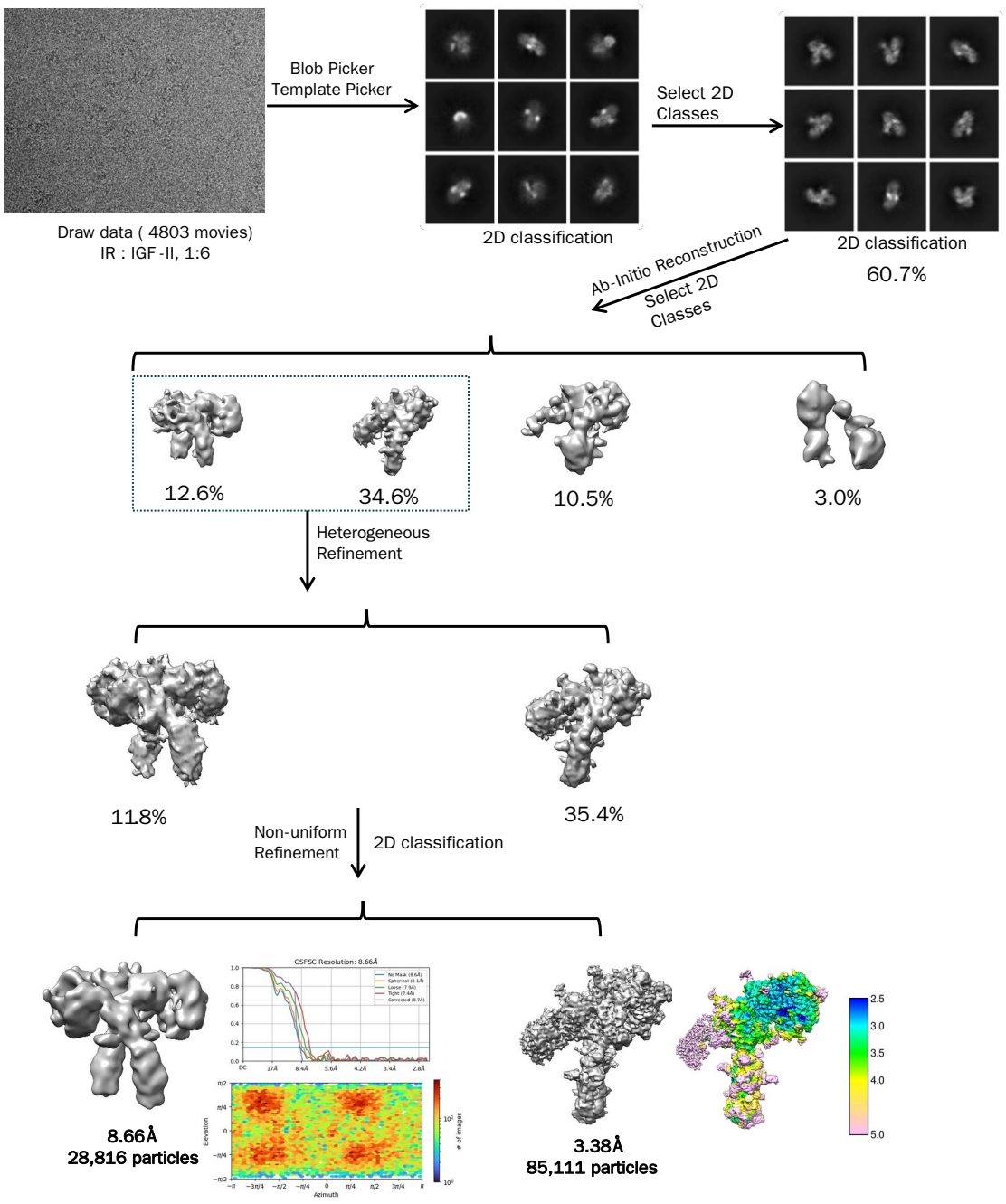

Fig. S7 Cryo-EM data processing flowchart of the IR/IGF-II mixture at a molar ratio of 1:6.

The fourier shell correlation curve and direction distribution plot of the final three-dimensional reconstructed map (low resolution) were showed next to the classical T shaped map, and the final high-resolution map was colored according to local resolution.

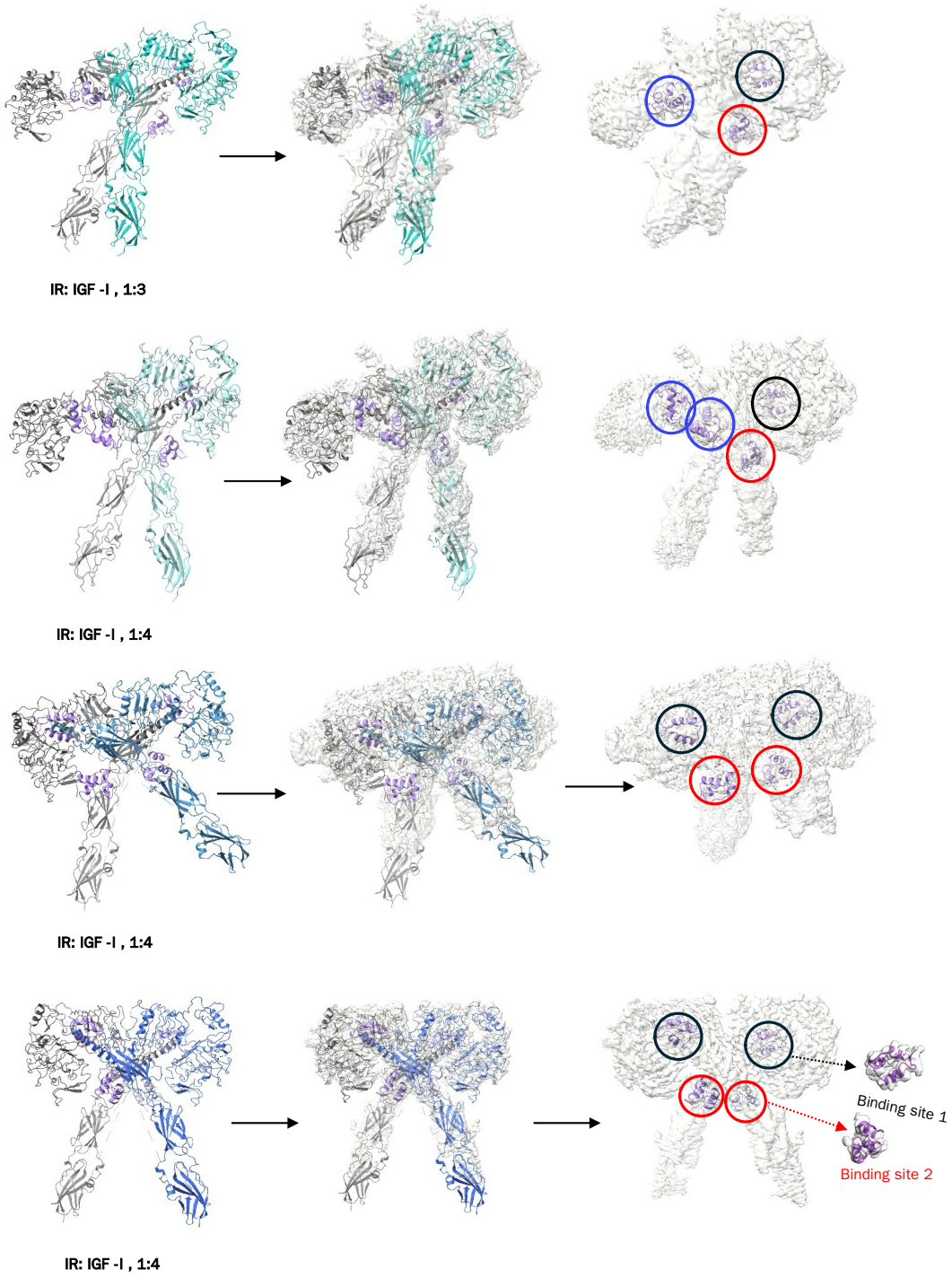

Fig. S8 Overall cryo-EM structures of the IR/IGF-I complexes.

The protomer A and IGF-I were colored as light gray and light purple, respectively. And the protomer B were colored as different colors with the conformational changes. Meanwhile, the IGF-I at binding site 1, site 2 and site 1/2 were marked by black, blue and red box, respectively.

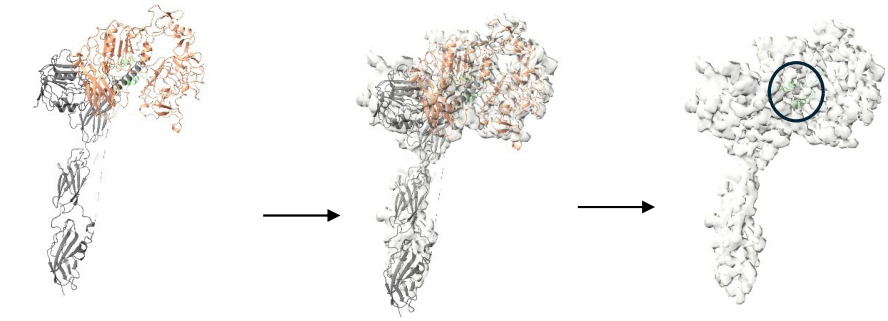

IR: Insulin , 1:1

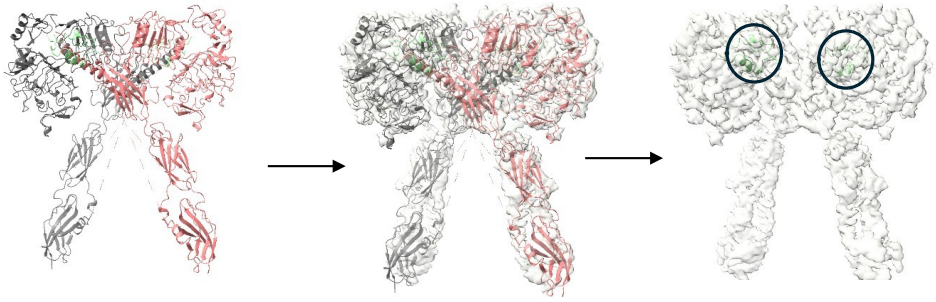

IR: Insulin , 1:2

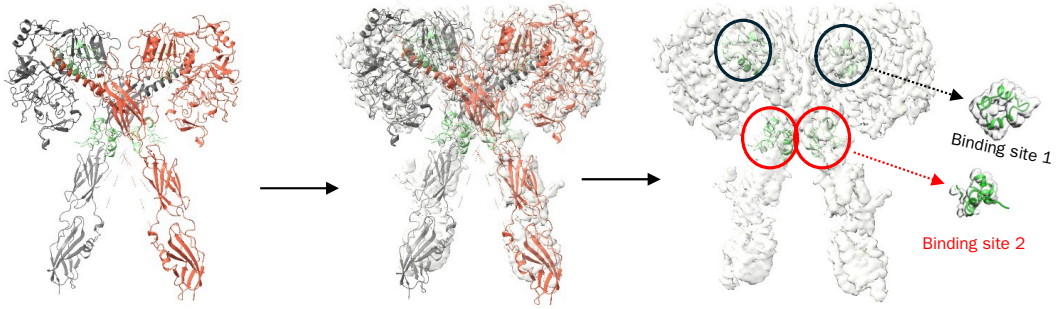

IR: Insulin , 1:4

Fig. S9 Overall cryo-EM structures of the IR/insulin complexes.

The protomer A, protomer B and Insulin were colored as light gray, orange and light green, respectively. And the insulin at binding site 1 and site 2 were marked by black and red box, respectively.

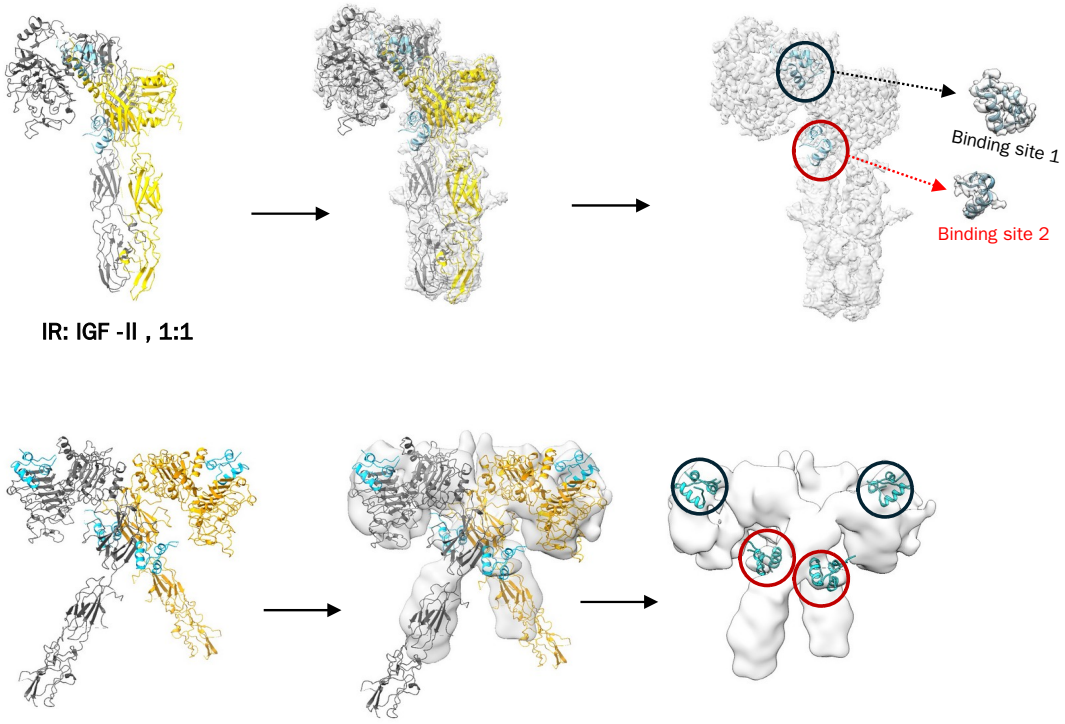

631

632 **Fig. S10 Overall cryo-EM structures of the IR/IGF-II complexes.**

633 The protomer A, protomer B and IGF-II were colored as gray, yellow and

634 cyan, respectively. And the IGF-II at binding site 1 and site 2 were

635 marked by black and red box, respectively.

636

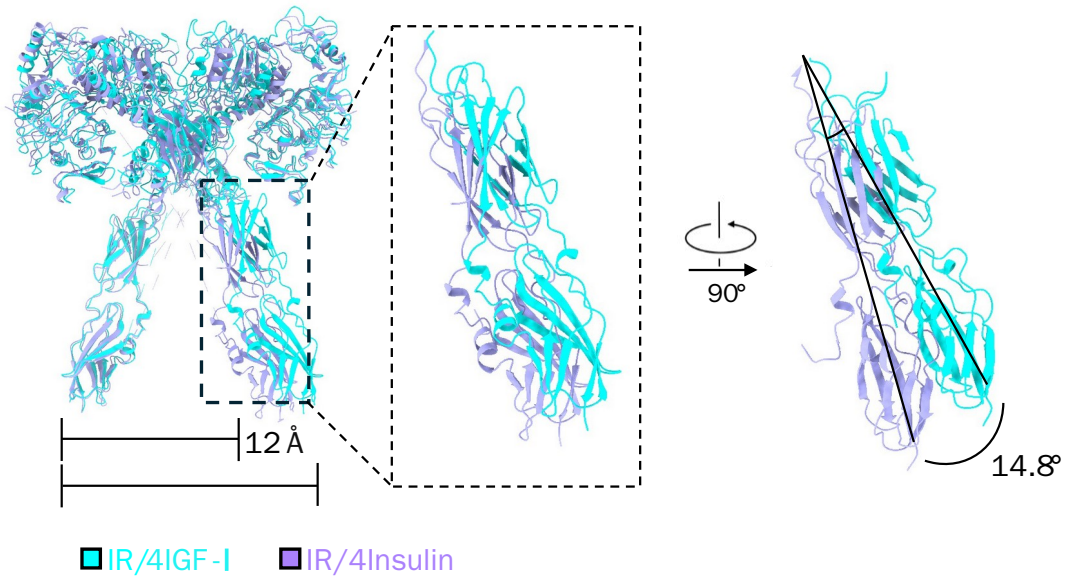

637

638 **Fig. S11 Comparison of symmetrical structures of the IR/4insulin**

639 **and IR/4IGF-I complexes.**

640 The IR/4insulin and IR/4IGF-I complexes were colored as cyan and light

641 purple, respectively.

642

643 **Table S1. Cryo-EM data collection, refinement and validation statistics for the IR/IGF-I,**

644 **IR/insulin and IR/IGF-II complex.**

	IR with 3 IGF-I	IR with 4 IGF-I, Conformation 1	IR with 4 IGF-I, Conformation 2	IR with 4 IGF-I, Conformation 3
Data collection and processing				
Magnification	130,000	130,000	130,000	130,000
Voltage (keV)	300	300	300	300
Electron exposure ($e^-/Å^2$)	50	50	50	50
Defocus range (μm)	1.5 to 2.5	1.5 to 2.5	1.5 to 2.5	1.5 to 2.5
Pixel size (Å)	0.66	0.66	0.66	0.66
Symmetry imposed	C1	C2	C1	C1
Initial particle images (no.)	137,8578	137,8578	137,8578	137,8578
Final particle images (no.)	148,338	133,029	85,221	82,568
Map resolution (Å)	3.24	3.31	3.53	5.00
FSC threshold	0.143	0.143	0.143	0.143
Map resolution range (Å)	2.2~999	2.2~999	2.2~999	2.2~999
Refinement				
Initial model used (PDB code)	AlphaFold2	AlphaFold2	AlphaFold2	AlphaFold2
Model resolution (Å)	3.7	3.6	4.0	9.27
FSC threshold	0.5	0.5	0.5	0.5

Map sharpening *B* factor (Å²)	-93.5	-81.9	-72.5	-88.4
Model composition				

Continued Table

	IR with 3 IGF-I	IR with 4 IGF-I, Conformation 1	IR with 4 IGF-I, Conformation 2	IR with 4 IGF-I, Conformation 3
Non-hydrogen atoms	14,171	14,724	14,455	14,019
Protein residues	1,765	1,834	1,802	1,742
Nucleotide base	0	0	0	0
B factor (Å²)				
Protein	186.16	200,02	341.74	412.12
Nucleotide	0	0	0	0
R.m.s. deviations				
Bond lengths (Å)	0.002	0.003	0.002	0.003
Bond angles (°)	0.526	0.726	0.654	0.724
Validation				
MolProbity score	1.71	2.01	2.15	2.41
Clash score	7.39	12.16	14.57	24.08
Poor rotamers (%)	0.13	0.30	0.19	0.95
Ramachandran plot				
Favored (%)	95.69	93.85	92.21	90.91
Allowed (%)	4.31	6.15	7.79	9.09

Disallowed (%)	0	0	0	0
PDB	8XJS	8XK1	8XKR	8XKM
EMDB	EMD-38404	EMD-38413	EMD-38423	EMD-38420

645 Continued Table

	IR with 1 insulin	IR with 2 insulin	IR with 4 insulin	IR with 2 IGF-II
Data collection and processing				
Magnification	130,000	130,000	130,000	130,000
Voltage (keV)	300	300	300	300
Electron exposure ($e^-/Å^2$)	50	50	50	50
Defocus range (μm)	1.5 to 2.5	1.5 to 2.5	1.5 to 2.5	1.5 to 2.5
Pixel size (Å)	0.66	0.66	0.66	0.66
Symmetry imposed	C1	C2	C2	C1
Initial particle images (no.)	58,2138	58,2138	51,2641	679,506
Final particle images (no.)	69,546	30,851	69,035	85,111
Map resolution (Å)	4.01	4.14	3.60	3.38
FSC threshold	0.143	0.143	0.143	0.143
Map resolution range (Å)	2.2~999	2.2~999	2.2~999	2.2~999
Refinement				
Initial model used (PDB code)	AlphaFold2	AlphaFold2	AlphaFold2	AlphaFold2
Model resolution (Å)	4.2	4.4	4.1	3.7

FSC threshold	0.5	0.5	0.5	0.5
Map sharpening *B* factor (Å^2)	-53.1	-85.5	-98.2	-67.9
Model composition				
Non-hydrogen atoms	9,107	13,710	14,147	10,912
Protein residues	1,126	1,702	1,757	1356

Continued Table

	IR with 1 insulin	IR with 2 insulin	IR with 4 insulin	IR with 2 IGF-II
Nucleotide base	0	0	0	0
B factor (Å^2)				
Protein	233.25	486.01	246.25	150.74
Nucleotide	0	0	0	0
R.m.s. deviations				
Bond lengths (Å)	0.003	0.004	0.003	0.004
Bond angles (°)	0.676	0.979	0.684	0.966
Validation				
MolProbity score	1.77	2.11	2.04	1.82
Clash score	11.58	11.99	14.57	6.23
Poor rotamers (%)	0.20	0.26	0.00	0.41
Ramachandran plot				
Favored (%)	96.88	91.12	94.65	92.34

Allowed (%)	3.12	8.88	5.35	7.66
Disallowed (%)	0	0	0	0
PDB	8YYL	8YYS	8YYT	8YSZ
EMDB	EMD-39675	EMD-39677	EMD-39678	EMD-39566